Simulation and analysis of 1.55 μm double-fused vertical-cavity lasers

Joachim Piprek[a)]
Materials Science Program, University of Delaware, Newark, Delaware 19716

Dubravko I. Babić
Hewlett-Packard Laboratories, 3500 Deer Creek Road, Palo Alto, California 94304

John E. Bowers
Department of Electrical and Computer Engineering, University of California, Santa Barbara, California 93106

(Received 19 July 1996; accepted for publication 16 December 1996)

Using a comprehensive numerical model, we analyze the first long-wavelength (1.55 μm) vertical-cavity surface-emitting lasers operating continuous-wave at room temperature (up to 33 °C). These double-fused lasers employ strain-compensated InGaAsP multi-quantum wells sandwiched between GaAs/AlGaAs distributed Bragg reflectors that are fused on both sides of the InP spacer. The two-dimensional model includes drift and diffusion of electrons and holes, finite-element thermal analysis, calculation of the internal optical field at threshold, and $\mathbf{k}\cdot\mathbf{p}$ band structure computations. The simulation shows excellent agreement with a large variety of experimental characteristics. Internal laser parameters like optical losses and injection efficiency are obtained. The thermal conductivity of the multilayer mirror is found to be only one third of the value expected. Temperature dependent absorption and Auger recombination within the active region as well as lateral leakage currents are identified as dominating loss mechanisms. The analysis shows great potential for high-temperature operation of double-fused vertical-cavity lasers. © *1997 American Institute of Physics.* [S0021-8979(97)00207-7]

I. INTRODUCTION

Long-wavelength (1.3–1.6 μm) vertical-cavity surface-emitting lasers (VCSELs) are a promising new generation of light sources for optical communication systems and optical interconnects. Compared to their edge-emitting counterparts, VCSELs are expected to exhibit advantages in testing, optical coupling, single-mode operation, and modulation. In contrast to the rapid development of AlGaAs VCSELs emitting at shorter wavelengths ($<1\,\mu$m)[1], continuous-wave (cw) lasing operation of long-wavelength InGaAsP VCSELs is severely limited by internal laser heating. This is mainly attributed to disadvantageous material properties of the InGaAsP semiconductor system at long wavelengths. With the lower band gap of the InGaAsP active region, Auger recombination enhances non-radiative losses. With lower photon energy, electron transitions from the split-off valence band into empty states of the heavy-hole band occur at sufficiently high hole densities, causing strong intervalence band absorption (IVBA). Both loss mechanisms are well known from edge-emitting lasers,[2] but they are even more severe in VCSELs since the lasing wavelength cannot follow the thermal shift of the gain peak. As a consequence, both the threshold current and the external quantum efficiency are very sensitive to changes in temperature. The use of InGaAsP/InP distributed Bragg reflectors (DBRs) within those VCSELs is accompanied by two additional hindering material properties. InGaAsP lattice matched to InP allows for a small variation of the refractive index that is only about half the variation possible in AlGaAs on GaAs. To obtain high DBR reflectances, a large number of mirror layers has to be grown causing significant diffraction losses.[3] InGaAsP also exhibits low thermal conductivity due to disorder scattering of phonons. Thus, thick InGaAsP/InP DBRs that block the thermal flux to the stage lead to a strong increase of the active region temperature in cw operation.

Several advanced concepts of long-wavelength VCSELs have been developed to overcome those limitations.[4–6] So far most successful is the utilization of InP/GaAs wafer fusion that led to cw operation of 1.55 μm VCSELs up to ambient temperatures of 33 °C.[7–9] These double-fused VCSELs will be further analyzed in our paper to identify the physical mechanisms that prevent lasing at higher temperatures.

The device structure is shown in Fig. 1. Thirty periods of $GaAs/Al_{0.67}Ga_{0.33}As$ form the top DBR that is covered by a metal contact on a GaAs phase matching layer to enhance reflectivity. The mirror absorption is kept small by using relatively low 4×10^{17} cm^{-3} beryllium p doping. The layer interfaces are parabolically graded to reduce interface electrical resistance.[10] The InGaAsP multi quantum well (MQW) active region consists of 7 QWs with about 1.0% compressive strain and 6 barriers with about 0.9% tensile strain. It is embedded in InP spacer layers that have been extended by thin GaAs layers on top of each fused mirror to increase the emission wavelength. The bottom 28-period GaAs/AlAs DBR is pulse doped at all interfaces, in addition to 10^{18} cm^{-3} silicon doping. The laser sits top-up on a copper stage, leaving a 2 mm hole for light output through the substrate. Further details of the laser are given in Table I including data from Ref. 7 as well as values that have been determined during the following simulation of experimental results.

The numerical VCSEL simulation combines thermal, optical, gain, and electrical models. Compared to previous versions,[11] the electrical model has been improved by two

a)Electronic mail: piprek@udel.edu

 0021-8979/97/81(8)/3382/9/$10.00

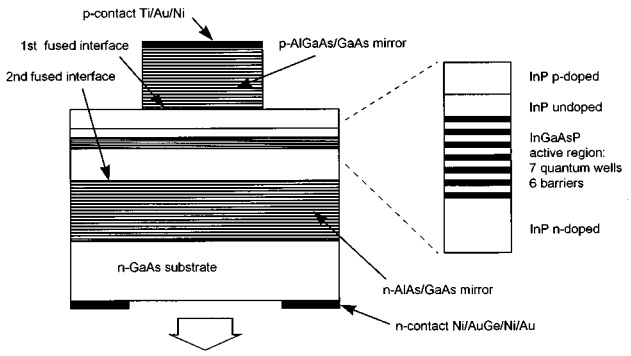

FIG. 1. Schematic structure of the double-fused vertical-cavity surface-emitting laser diode analyzed.

dimensional (2D) finite-element analysis of drift and diffusion of electrons and holes across semiconductor heterointerfaces, that is required to thoroughly investigate current leakage. Most other advanced VCSEL models published consider drift only outside the active region and diffusion only inside the active region (see, e.g., Refs. 12 and 13). Details of our theoretical models are described in Section II including a discussion of physical processes and material parameters. These models are used independently or combined appropriately to simulate a variety of measured device characteristics. The results of these simulations strongly depend on specific material properties and those parameters are determined by fitting experimental data. In Section III, pulsed and cw operation at laser threshold are analyzed and the question is answered how to achieve cw lasing well above room temperature.

II. MODELS AND MATERIAL PARAMETERS

A. Thermal simulation

A 3D finite-element code[14] is used to solve the steady-state heat conduction equation and to obtain the cylinder symmetrical temperature distribution $T(r,z)$ within the VCSEL. The bottom metal contact has the constant stage temperature T_s and heat flux through any other surface is neglected. In general, the temperature rise depends sensitively on the local distribution of the heat generation as function of the injection current I. In our simple case, the top p-DBR pillar produces most of the internal heat power due to electrical interface resistances at the metal-semiconductor contact, within the DBR, and at the fused GaAs/InP interface. Interface resistances involve quantum-mechanical carrier tunneling that strongly depends on the electrostatic potential profile, i.e., on the local distribution of dopants. Calculations of the interface resistance based on the Schrödinger–Poisson system of equations show poor agreement with measurements due to uncontrolled Be diffusion within the p-DBR. Thus, measured voltage vs. current characteristics $V(I)$ of our example device are used to determine the total pillar resistance (Fig. 2). It is of minor importance here, to distinguish between the different types of interfaces since all the pillar heat follows the same path through the active region to the stage. Figure 2 shows that the cw voltage is smaller than the pulsed voltage due to the effect of pillar heating on the interface resistance. $V(I)$ is reduced by the active region Fermi level separation $V_a \approx 0.8$ V to calculate the pillar electrical resistivity ϱ as function of the current density j. The fit results in a resistivity $\varrho(j)$ [Ω cm^2] that decreases with rising current density j [A/cm^2] according to

$$\varrho(j) = 0.36 \times j^{-0.75}, \tag{1}$$

but the total pillar heat power rises with $I^{1.25}$. The electrical resistance of the bottom n-DBR is negligible compared to that of the top pillar. The active region heat power is IV_a, the net photon emission is neglected near threshold.

Bulk thermal conductivities are applied to all layers, except the DBRs. Here, reduced values are expected that are caused by phonon mean free path restrictions in thin layers. Measurements on AlGaAs VCSELs result in a thermal conductivity that is only 20% of the average bulk value.[15] Due to

TABLE I. Internal parameters of the double-fused VCSEL at 25 °C as used in the simulation (l layer thickness, N_{dop} doping, μ majority carrier mobility, n refractive index, dn/dT temperature coefficient of n, α absorption coefficient, and κ thermal conductivity. * indicates values that have been adjusted to fit experimental results).

Parameter Unit	l (μm)	N_{dop} (1/cm^3)	μ (cm^2/V s)	n	dn/dT (10^{-4}/K)	α (1/cm)	κ (W/cm K)
Au/Ti (contact)	0.200	⋯	⋯	0.83		684000	0.67
p-GaAs	0.020	2×10^{19}	⋯	3.38	3*	500	0.44
p-GaAs	0.182	4×10^{17}	⋯	3.38	3*	25*	0.22*
p-$Al_{0.67}Ga_{0.33}As$ (DBR)	0.127	4×10^{17}	⋯	3.05	2	25*	0.22*
p-GaAs (DBR)	0.115	4×10^{17}	⋯	3.38	3*	25*	0.44
p-GaAs (spacer)	0.020	4×10^{17}	⋯	3.38	3*	25*	0.44
p-GaAs (spacer)	0.010	4×10^{19}	⋯	3.38	3*	1000	0.44
p-InP (spacer)	0.178*	1×10^{18}	30*	3.17	2	24	0.68
p-InP (spacer)	0.100	1×10^{16}	150	3.17	2	0.24	0.68
$In_{0.76}Ga_{0.24}As_{0.82}P_{0.18}$ (QW)	0.0055*	⋯	100	3.6	2	54*	0.043
$In_{0.48}Ga_{0.52}As_{0.82}P_{0.18}$ (barrier)	0.008	⋯	100	3.4	2	54*	0.043
n-InP (spacer)	0.258*	5×10^{18}	4600	3.15	2	8	0.68
n-GaAs (spacer)	0.050	1×10^{18}	⋯	3.38	3*	6	0.44
n-GaAs (DBR)	0.115	1×10^{18}	⋯	3.38	3*	6	0.22*
n-AlAs (DBR)	0.134	1×10^{18}	⋯	2.89	1	3	0.22*
n-GaAs (substrate)	450	5×10^{18}	⋯	3.38	3*	5.8	0.44

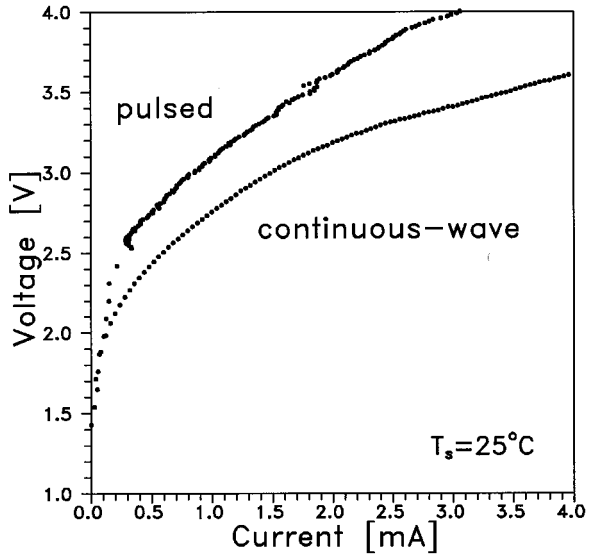

FIG. 2. Measured voltage vs current characteristics $V(I)$ of the double-fused VCSEL in pulsed and in cw operation ($d=12$ μm) (see Ref. 7).

this uncertainty, the thermal conductivity of the n-DBR is used as fit-parameter to find agreement with the measured threshold current $I_{th}(T_s)$ in cw operation (see Sec. III B), resulting in $\kappa_{DBR}=0.22$ W/cm K, one third of the average bulk value. The same parameter is applied to the top DBR where its impact is small with top-up mounting. All other thermal conductivities in Table I are taken from Ref. 16 and an average temperature dependency of $\kappa \propto T^{-1.375}$ (Ref. 17) is included.

The laterally averaged temperature rise $\Delta T_a(I)$ within the active region divided by the total heat power IV gives a thermal VCSEL resistance of 1440 K/W that slightly increases with rising I, mainly due to the thermal lowering of $\kappa(T)$.

The calculated temperature profile $T(0,z)$ and the average MQW temperature T_a are employed in the following simulation steps as function of the injection current I.

B. Optical simulation

In general, the calculation of the three-dimensional electromagnetic field within a VCSEL requires elaborate solutions of Maxwell's equations in an open resonator.[18,19] In many cases, the effective index method can be used to investigate the behavior of higher-order transverse modes in VCSELs.[12]

In this work, we are primarily interested in lasing operation at threshold. Therefore, mode shape, resonant wavelength and modal gain are determined using a simplified analysis. Our air-post structure shows strong index guiding and considerable sidewall scattering. Thus, the lowest-order transverse mode is assumed to be the first to reach threshold. The air-post is modeled as a cylindric dielectric waveguide leading to Bessel functions approximately describing the field both in and below the pillar. Spatial hole burning is expected only at higher photon densities well above threshold and it is not considered here. Furthermore, we assume that thermal lensing is negligible in our case of homogeneous current injection through the DBR pillar.

The reflectivity of the air-post pillar seen from the cavity is calculated assuming normal incidence. The resonant wavelength λ and the threshold gain g_{th} of this cavity are determined using the transmission matrix method.[20] The cavity losses resulting from scattering on the DBR pillar sidewalls are added to the DBR absorption. The free-space propagation of the mode through the bottom part of the VCSEL results in diffraction loss when the mode couples back to the air-post pillar.[3] This diffraction loss is expected to be very small, as shown in Ref. 7. The differential external quantum efficiency

$$\eta_{ext}=\eta_i|E_{out}|^2/g_{th}l_a n_a|E_a|^2 \tag{2}$$

is calculated from the intensity ratio $|E_{out}|^2/|E_a|^2$ of emitted wave and average optical field within the active region with $l_a n_a$ describing the optical length of the active region.[21] The differential carrier injection efficiency η_i is later found to be 80% (see Section III A). Table I lists the material parameters n, dn/dT, and α that are essential for the optical simulation. These values shall now be discussed in detail. Critical parameters are obtained by fitting the optical simulation to measured characteristics of emission wavelength and differential external efficiency.

The refractive indices n of AlGaAs, InP, and the metal contact are obtained from Refs. 22–24, respectively. Within the MQW active region, n is influenced by the carrier density and approximated values are used here (variations show only small effect). The temperature dependency $n(T)$ has been found to have considerable impact on VCSEL performance.[21] Material dependent temperature parameters dn/dT cause a thermal shift not only of the emission wavelength, but also of DBR reflectivity, external efficiency, and threshold gain. Values of dn/dT are extracted from Ref. 23 (InP) and Ref. 25 (AlAs). Varying numbers dn/dT are reported for GaAs and the measured thermal red-shift of the lasing wavelength $d\lambda/dT_s \approx$ 0.12 nm/K in pulsed VCSEL operation is used to obtain $dn/dT=3\times10^{-4}$ K^{-1}. From those parameters, the refractive index of each layer is determined according to the temperature profile $T(0,z)$ as function of the injection current I. Thermal expansion of the layer thicknesses is also included but its influence is negligible.

At $T_s=25$ °C, the measured emission wavelength is $\lambda = 1542$ nm. This number is governed by the optical length of the cavity. Before fusion, thin GaAs layers have been added on top of each mirror to increase λ and to compensate for small InP spacer layers.[7] Inhomogeneities of several 10 nm are not surprising in InP wafer fabrication. In the optical calculation, the InP spacer thicknesses are fitted to find agreement with the measured wavelength. Slight deviations of other layer thicknesses or of refractive indices are also possible but hard to separate.

Photon absorption is mainly caused by free carriers and the absorption coefficients α are obtained from Ref. 7, except for the p-DBR and the MQW. In the p-DBR pillar, scattering losses at the sidewall have to be added to the average bulk absorption of 8 cm^{-1}. These sidewall losses can be extracted from the measured external efficiency at different pillar diameters d.[26] The differential injection efficiency

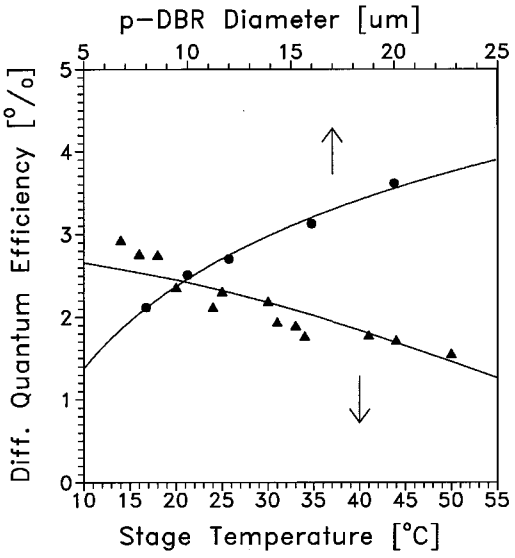

FIG. 3. Differential external quantum efficiency η_{ext} vs stage temperature T_s ($d=12$ μm) and vs. top DBR diameter d ($T_s=23$ °C) in pulsed operation: comparison of measurement (see Ref. 7) (dots) and simulation (lines).

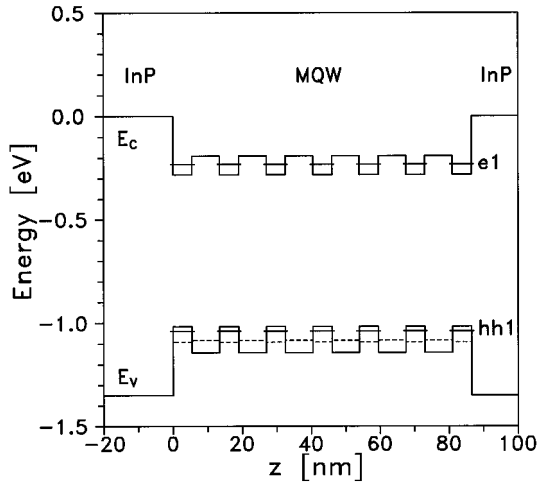

FIG. 4. Strain-compensated multi-quantum well active region: conduction band edge E_c, valence band edge E_v for heavy holes (solid) and light holes (dashed), and first energy levels for electrons and holes, respectively.

η_i is almost constant as indicated by recent measurements.[27] The fit to the experimental characteristic $\eta_{ext}(d)$ (Fig. 3) results in an almost linear dependency of the p-DBR optical losses α_{p-DBR} [1/cm] on d^{-2} [cm^{-2}]

$$\alpha_{p-DBR}=8+2.39\times10^{-5}/d^2. \tag{3}$$

For our example device ($d=12$ μm), the measured external quantum efficiency is only about 2.3% at 25 °C and it shows an exponential decrease with rising temperature (Fig. 3). This behavior must be related to temperature dependent absorption somewhere in the VCSEL (the influence of carrier leakage is discussed in Section III A). Intervalence band absorption shows an exponential temperature dependency based on the number of heavy holes that are available at the IVBA wavevector.[2] IVBA is also proportional to the total hole density. Within the MQW active region, the hole density at threshold is known to increase with higher temperature. Thus, an exponential temperature dependency of the MQW absorption coefficient α_{MQW} [1/cm] is assumed and the fit to measured data $\eta_{ext}(T_s)$ (Fig. 3) gives

$$\alpha_{MQW}=1.57\times10^{10}\exp\left[\frac{-0.5\ \text{eV}}{kT_a}\right] \tag{4}$$

(k is Boltzmann constant). The effective activation energy of 0.5 eV includes the increase in threshold carrier density and it is larger than the IVBA activation energy.[2] The MQW absorption coefficient at 25 °C is 54 cm^{-1}. Because of additional loss mechanisms considered here, this number is smaller than reported previously[11] and it is now in excellent agreement with IVBA measurements on compressively strained 1.55 μm MQWs.[28] The accuracy of our MQW absorption parameters depends on the accuracy of the optical losses assumed in the other layers. The highly doped p-side GaAs/InP interface could also cause strong IVBA, but it is intentionally close to the null of the optical field and its impact on the loss calculations is small. This impact could rise due to uncontrolled dopant diffusion away from the interface causing absorption losses that can hardly be separated from MQW absorption in our device analysis. Thus, Eq. (4) is considered to represent the net effect of temperature dependent absorption in the VCSEL investigated.

C. Gain calculation

The objective of the gain model is to calculate the threshold carrier density N_{th} from the threshold gain g_{th} obtained in the optical simulation. The gain computation was developed from Ref. 29 and it includes two steps. First, the energy band structure of the strain-compensated MQW is determined using a 4×4 $\mathbf{k}\cdot\mathbf{p}$ method[30] and the band offset model of Ref. 31. Both the hydrostatic and the shear component of the strain change the valence band structure. Figure 4 displays the energy band diagram of our MQW including the first energy level of electrons and holes, respectively. In the valence band, the band edge is different for heavy holes and light holes. Light holes are not localized in the quantum well. Dipole matrix elements of all transitions between conduction and valence bands are obtained. In the second step, the optical gain $g(\lambda,N,T_a)$ is calculated from those results for any given emission wavelength λ, MQW carrier density N, and average active region temperature T_a. Thereby, we calculate first the spontaneous emission spectrum R_{spon} using the stored band structure, dipole matrix elements, and a Lorentzian broadening with an intraband relaxation time of 10^{-13} s.[2] Then, the optical gain is determined via the relation

$$g(\lambda,N,T_a)\propto\left[1-\exp\left(\frac{hc/\lambda-eV_a(N,T_a)}{kT_a}\right)\right]\times R_{spon}(\lambda,N,T_a), \tag{5}$$

where eV_a is the separation between the quasi-Fermi energies of holes and electrons and hc/λ is the photon energy (h is Planck's constant, c is light velocity).

The calculated gain depends on MQW layer compositions and thicknesses which might be slightly different from

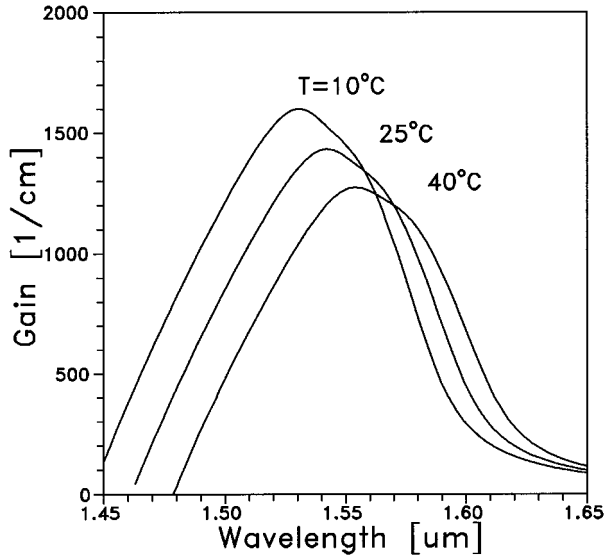

FIG. 5. Optical gain $g(\lambda,N,T_a)$ as function of the emission wavelength λ with the MQW temperature T_a as parameter ($N=3\times10^{18}$ cm^{-3}).

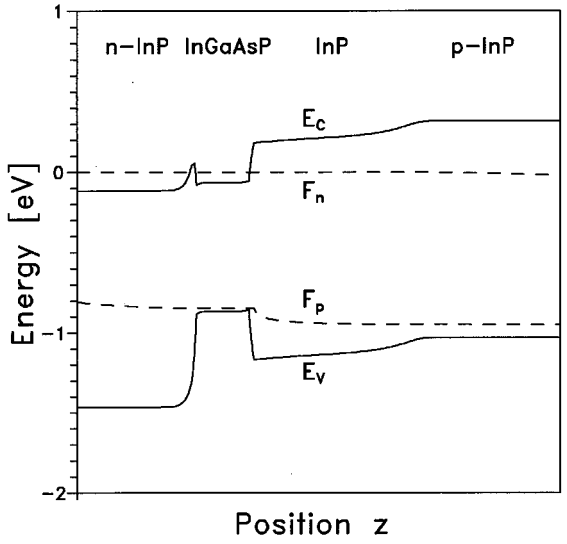

FIG. 7. Energy band diagram near the InGaAsP active region as calculated in the electrical model near threshold (F_n, F_p—quasi Fermi levels of electrons and holes).

the numbers intended. Both parameters affect the QW band gap which has to be adjusted to fit experimental results. In our case, the intended QW thickness of 6 nm is reduced by 0.5 nm to find agreement with the peak of the photoluminescence spectrum measured before fusion.[7] The thermal band gap shrinkage parameter used is $dE_g/dT=-0.37$ meV/K,[17] and it governs the red-shift of the gain spectrum with higher temperature (Fig. 5). This shift of the gain peak is stronger than the shift of the emission wavelength, causing a substantial decrease of the gain at higher temperatures. Calculated functions $g(\lambda)$ for different carrier densities N at $T_a=25\,^{\circ}$C are depicted in Fig. 6. At small carrier densities, increasing band filling causes a blue-shift of the gain peak wavelength and at higher N, carrier exchange and correlation effects lead to a gain peak red-shift (band gap shrinkage).

At threshold, the lateral carrier distribution within the MQW is almost homogeneous underneath the DBR pillar and the condition $g_{th}=g(\lambda,N_{th},T_a)$ delivers the threshold carrier density N_{th}.

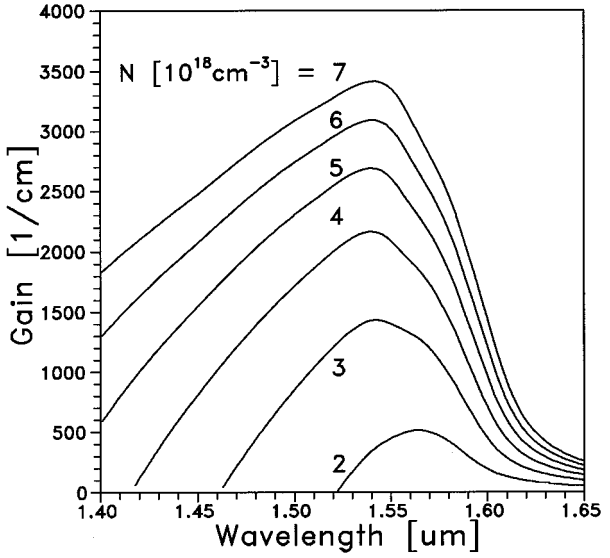

FIG. 6. Optical gain $g(\lambda,N,T_a)$ as function of the emission wavelength λ with the MQW carrier density N as parameter ($T_a=25\,^{\circ}$C).

D. Electrical simulation

This part of the simulation procedure eventually delivers the threshold current I_{th} corresponding to the threshold carrier density N_{th} calculated above. The carrier transport through the double-fused VCSEL is affected by a large number of hetero-interfaces, especially within the DBRs, that create a considerable electrical resistance. This resistance depends on current density and temperature (Fig. 2). The total voltage drop is mainly determined by the top pillar (including the upper fused interface) and by the Fermi level split in the active region ($V_a\approx0.8$ V). In our electrical model, the homogeneous current injection through the p-DBR pillar on one side and the small n-DBR resistance and high electron mobility on the other side allow for the separation of the center part of the VCSEL from the DBRs with the two fused interfaces considered as injection contacts. The carrier transport through spacer layers and active region is simulated by solving the van Roosbroeck equations[32] for drift and diffusion of electrons and holes using a 2D finite element code.[33] This code considers Fermi statistics and hetero-interfaces but it does not yet include quantum wells. Thus, a 38.5 nm thick bulk active region is assumed with effective densities of states in conduction and valence band, $N_c=5.5\times10^{17}$ cm^{-3} and $N_v=5.0\times10^{18}$ cm^{-3}, respectively, which have been obtained from the MQW band structure calculations. These numbers ensure that the positions of the quasi Fermi levels within the bulk active region near threshold correspond to our strain-compensated MQW (Fig. 7). The con-

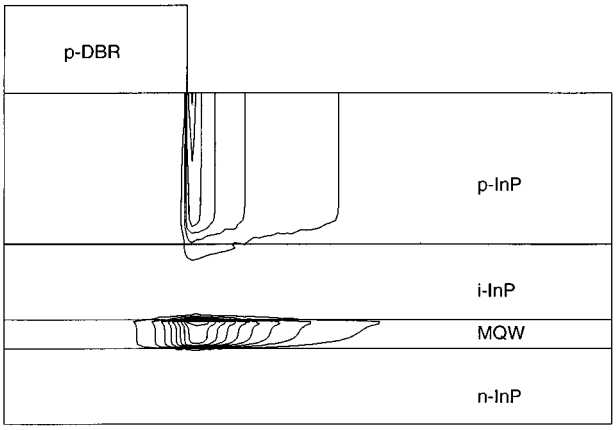

FIG. 8. Contour plot of the hole current density $j_{p,r}(r,z)$ in r-direction near the p-DBR pillar rim.

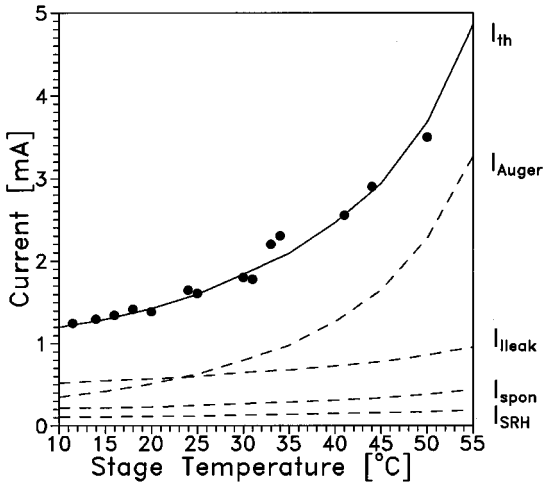

FIG. 9. Threshold current I_{th} vs stage temperature T_s in pulsed operation: comparison of measurement (see Ref. 7) (dots) and simulation (solid line). Dashed lines show the contribution of different mechanisms according to Eq. (6).

duction band discontinuity of 0.23 eV is chosen equal to the difference between the InP conduction band edge and the first electron level within the quantum wells (Fig. 4). Doping densities and mobilities are given in Table I. Other important material parameters of the electrical model are the rate coefficients A and C of Shockley–Read–Hall (SRH) recombination and Auger recombination, respectively. Both are obtained from fits to measurements (Section III A). The results $A=7\times10^{7}$ s^{-1} and $C=10^{-28}$ cm^6/s agree with numbers typically reported. The activation energy of the Auger process is assumed to be 0.1 eV. The MQW recombination rate due to spontaneous emission is given by R_{spon}.

This 2D carrier transport model is suitable to investigate the leakage current that does not contribute to carrier recombination within the active region. In general, two leakage mechanisms can be distinguished: vertical and lateral leakage.

Vertical leakage is caused by carriers that leave the active region in the z direction by thermionic emission. The band diagram in Fig. 7 shows that the leakage of electrons into the lowly doped p-spacer is more likely than the leakage of holes in opposite direction. This electron leakage strongly depends on the position of the electron Fermi level, i.e., on the threshold density N_{th}.

Lateral leakage currents in r direction can be caused in two different ways. First, by lateral diffusion of MQW carriers away from the the active region underneath the DBR pillar. This ambipolar diffusion process is dominated by the diffusivity of holes. Second, lateral hole drift away from the DBR pillar occurs within the upper 10^{18} cm^{-3} p-doped InP spacer layer and it is enhanced by the low conductivity of the 10^{16} cm^{-3} p-doped InP layer underneath. This current spreading depends on the hole mobility μ_p within the upper spacer layer and it increases with lower p-DBR diameter d. The fit to the threshold current density curve $j_{th}(d)$ delivers $\mu_p=30$ cm^2/V s (see Section III A). This hole mobility of the upper InP layer is slightly lower than usually reported for InP due to the impact of the p-DBR reactive ion etching. Both lateral leakage currents can be clearly distinguished in Fig. 8 that plots the 2D distribution of the lateral hole current density $j_{p,r}(r,z)$ as calculated using the 2D drift-diffusion model.

In summary, the injection current I_{th} required to obtain the threshold carrier density N_{th} within the MQW active region depends on SRH recombination, spontaneous emission, Auger recombination, vertical leakage, and lateral leakage

$$I_{th}=I_{SRH}+I_{spon}+I_{Auger}+I_{vleak}+I_{lleak}. \tag{6}$$

The relative contribution of each mechanism to the threshold current and to its temperature dependency is analyzed in Section III.

III. SIMULATION AND ANALYSIS OF DEVICE PERFORMANCE

A. Pulsed operation

In pulsed operation, significant laser heating can be avoided. With our pulse length of 100 ns and a repetition rate of 100 kHz, no thermal shift of the emission wavelength occurs, compared to lower repetition rates. Thus, the internal laser temperature is approximately equal to the stage temperature T_s. The thermal simulation can be skipped and a constant temperature $T(r,z)\equiv T_s$ is assumed.

Measurements of the pulsed threshold current I_{th} of our example device show a strong dependency on the stage temperature T_s leading to a temperature coefficient of $T_o=44$ K (Fig. 9). Combining the optical, gain, and electrical model, $I_{th}(T_s)$ can be simulated by adjusting the non-radiative MQW recombination parameters A and C (solid line in Fig. 9). At $T_s=25\,^{\circ}$C, the threshold gain is found to be $g_{th}=900$ cm^{-1} and the threshold carrier density is $N_{th}=2.7\times10^{18}$ cm^{-3}. About 40% of the current is due to Auger recombination, 38% to lateral current leakage, 14% to spontaneous emission, and 8% to SRH recombination. The contribution of vertical current leakage is well below 1%. The dashed lines in Fig. 9 indicate the thermal increase of the different carrier losses. Auger recombination shows the

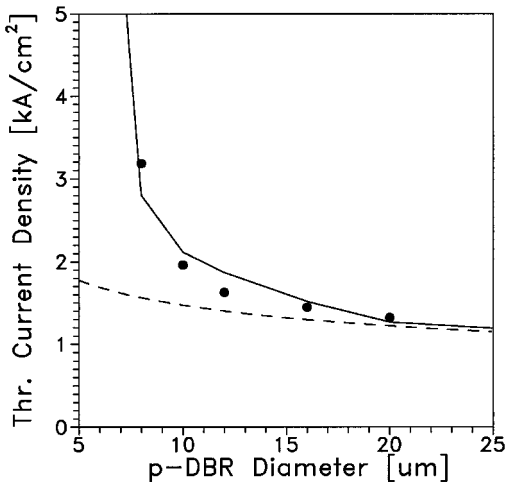

FIG. 10. Threshold current density j_{th} vs p-DBR diameter d in pulsed operation: comparison of measurement (see Ref. 7) (dots) and simulation (solid line). The dashed line shows the simulation without lateral leakage current.

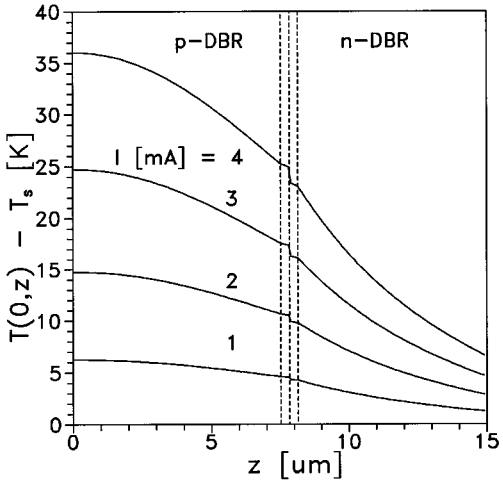

FIG. 11. Temperature increase along laser axis as calculated in the thermal simulation at different injection currents I.

strongest increment which is connected to the rising MQW absorption. The lateral leakage current is almost proportional to N_{th} and its increase is dominated by lateral hole diffusion within the MQW. Considerable vertical leakage only occurs at even higher temperatures with $N_{th}>5\times10^{18}$ cm^{-3}.

Measured values of the threshold current density j_{th} as function of the p-DBR diameter d are shown in Fig. 10. The fit (solid line) is obtained by adjusting the hole mobility in the upper p-InP spacer layer. The dashed line in Fig. 10 is based on the d-dependence of optical losses only. The difference between both curves gives the contribution of current spreading, that rises strongly with lower DBR diameter.

Besides contributing to the threshold current, carrier losses can also affect η_{ext} by reducing the differential MQW injection efficiency η_i. This influence is negligible only as long as the pulsed threshold current does not change above threshold, i.e., as long as the carrier losses are constant.[20] This is generally assumed for recombination and lateral diffusion losses within the active region since Fermi levels and carrier densities are clamped at the threshold level. But thermionic emission has been found to increase above threshold due to further reduction of the potential barrier within the p-spacer and to reduce η_i in 1.3 μm InGaAsP edge-emitting lasers.[34] In our case, no separate confinement layers are used and the large conduction band offset between MQW and InP keeps vertical leakage as well as its impact on η_i very small. Another carrier loss mechanism, that is not constant above threshold, is the lateral leakage in the upper p-InP spacer layer which strongly contributes to the total current. Since this hole drift current is driven by the electrical field, it increases with rising voltage and leads to $\eta_i=80\%$ for our example device.

The very good agreement of the simulations with a variety of measurements in pulsed operation confirms the physical parameters obtained. The same parameters are now employed to simulate cw operation.

B. Continuous-wave operation

cw operation causes a strongly inhomogeneous temperature distribution $T(r,z)$ within the VCSEL. The calculated temperature profile $T(0,z)$ along the laser axis is shown in Fig. 11 at different values of the injection current. A steep slope of $T(0,z)$ is caused by the low MQW thermal conductivity (at center dashed line in Fig. 11).

Measured cw threshold parameters I_{th} and η_{ext} are shown in Fig. 12 as a function of the stage temperature T_s. Lasing operation cannot be obtained for $T_s>33\,^{\circ}$C. All four components of the simulation procedure are combined to simulate this behavior, using the DBR thermal conductivity κ_{DBR} as the only fit parameter (see Section II A). After adjusting κ_{DBR}, the calculated functions $\eta_{ext}(T_s)$ and $I_{th}(T_s)$ are close to the data measured (Fig 12). Deviations might be caused by unstable heat sinking. In the calculation, no cw lasing occurs at temperatures $T_s>30\,^{\circ}$C, i.e., the required

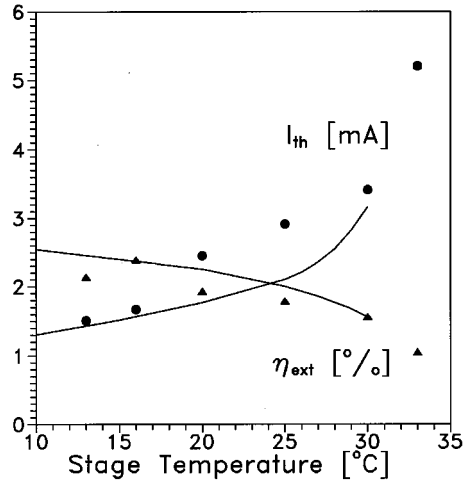

FIG. 12. Threshold current I_{th} and differential external quantum efficiency η_{ext} vs stage temperature T_s in cw operation: comparison of measurement (see Ref. 7) (dots) and simulation (lines).

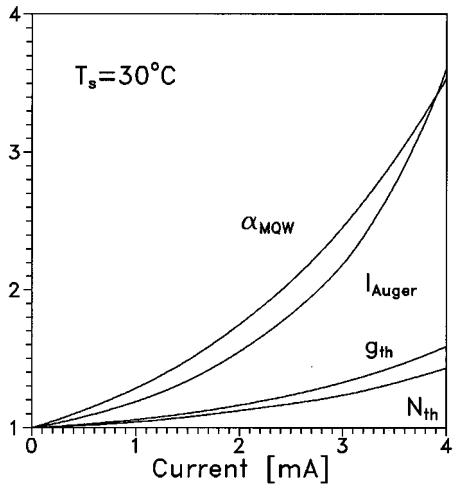

FIG. 13. Relative increase of MQW absorption α_{MQW}, Auger current I_{Auger}, threshold gain g_{th}, and threshold carrier density N_{th} with rising injection current I in cw operation at $T_s=30\,°\mathrm{C}$ (normalized to values in pulsed operation).

threshold current $I_{th}(I)$ remains larger than the injection current because of increased losses. This maximum stage temperature of 30 °C is correlated to a maximum temperature of the active region of 50 °C. Both numbers are in good agreement with experimental limits of 33 °C and 55 °C, measured in cw and in pulsed operation, respectively. At the maximum cw operation temperature, 58% of the threshold current are caused by Auger recombination, 25% by lateral carrier leakage, and only 1% by vertical electron leakage across the MQW. Figure 13 displays the relative increase of MQW absorption, threshold gain g_{th}, threshold density N_{th}, and Auger current I_{Auger} as functions of the injection current I at $T_s=30\,°\mathrm{C}$. With rising I, the MQW heats up and strongly enhanced MQW absorption ($\alpha_{MQW}=250\ \mathrm{cm}^{-1}$ at $T_a=50\,°\mathrm{C}$) leads to rising g_{th} and N_{th} (slightly counteracted by increased DBR reflectivity) and eventually to a large Auger current that keeps I_{th} above the injection current at higher temperatures. Thus, absorption losses are found to be the main reason for the temperature limitation of cw VCSEL operation. IVBA at 1.55 μm wavelength is known to be strong in bulk InGaAsP but it is often expected to decrease within compressively strained QWs.[35] Other investigations confirm considerable IVBA in 1.2% compressively strained 1.55 μm MQWs.[28] In our strain-compensated MQW, unconfined holes might enhance absorption losses (see Section II C).

Our analysis of device performance shows the great potential of double-fused VCSELs to achieve cw operation well above room temperature. Further investigation of absorption mechanisms in the strain-compensated MQW is expected to lead to an optimized MQW design. This should include a blue-shift of the gain spectrum to obtain a minimum of the threshold current above room temperature. Besides the MQW, several other possible improvements are obvious: (1) top-down mounting of the device significantly reduces the thermal resistance and cw operation up to 50 °C is simulated with our example device; (2) further reduction of the p-DBR heating, e.g., by using carbon dopants that tend to result in lower interface resistance than beryllium; (3) restriction of the lateral leakage current shall considerably reduce the threshold current and increase the injection efficiency; (4) the reduction of optical scattering losses by lateral p-DBR oxidation allows for lower active region diameters d_a and cw operation up to 64 °C has been achieved very recently at $d_a=8\,\mu$m.[27] A combination of those improvements is expected to lead to cw operation at 80 °C, which is a critical margin for practical applications of double-fused VCSELs.

IV. SUMMARY

Our comprehensive numerical VCSEL model includes all major loss mechanisms that potentially limit the device performance: temperature dependent optical absorption, p-DBR scattering losses, MQW non-radiative recombination, as well as vertical and lateral leakage currents. Internal material parameters are carefully adjusted and the simulation leads to an excellent agreement with a large variety of measured results. These measurements are: (1) threshold current vs temperature and vs DBR diameter, (2) differential external quantum efficiency vs temperature and vs DBR diameter, (3) emission wavelength vs temperature, and (4) voltage vs current. Internal laser parameters are determined, including the p-DBR electrical resistivity, optical losses in MQW and DBR, the injection efficiency (absolute and differential), the p-spacer hole mobility, the Auger coefficient, the thermal resistance, and the DBR thermal conductivity. Optical absorption, Auger recombination, and lateral leakage currents are found to be the main loss mechanisms. Intervalence band absorption dominates the thermal VCSEL behavior and it restricts the cw lasing temperature. The analysis clearly shows the potential of double-fused VCSELs for high-temperature cw operation.

ACKNOWLEDGMENTS

Valuable discussions with Dr. Hans Wenzel (Ferdinand Braun Institute, Berlin) and with Dr. Klaus Streubel (Royal Institute of Technology, Stockholm) are gratefully acknowledged. This work was supported in part by ARPA and by Rome Laboratories.

[1] T. E. Sale, *Vertical Cavity Surface Emitting Lasers* (Wiley, New York, 1995).
[2] *Handbook of Semiconductor Lasers and Photonic Integrated Circuits*, edited by Y. Suematsu and A. R. Adams (Chapman & Hall, New York, 1994).
[3] D. I. Babić, Y. Chung, N. Dagli, and J. E. Brown, J. Quantum Electron. **29**, 1950 (1993).
[4] T. Baba, Y. Yogo, K. Suzuki, F. Koyama, and K. Iga, Jpn. J. Appl. Phys. 1 **33**, 1905 (1994).
[5] C. L. Chua, Z. H. Zhu, Y. H. Lo, R. Bhat, and M. Hong, Photon. Technol. Lett. **7**, 444 (1995).
[6] K. Streubel, S. Rapp, J. Andre, and J. Wallin, Photon. Technol. Lett. **8**, 1121 (1996).
[7] D. I. Babić, Ph.D. dissertation, ECE Technical Report 95-20, University of California at Santa Barbara, 1995.
[8] D. I. Babić, K. Streubel, R. P. Mirin, N. M. Margalit, J. E. Bowers, E. L. Hu, D. E. Mars, L. Yang, and K. Carey, Photon. Technol, Lett. **7**, 1225 (1995).
[9] D. I. Babić, K. Streubel, R. P. Mirin, J. Piprek, N. M. Margalit, J. E.

Bowers, E. L. Hu, D. E. Mars, L. Yang, and K. Carey, Proceedings of the 8th International Conference on InP and Related Materials, 1996, p. 719.
[10] M. G. Peters, B. J. Thibeault, D. B. Young, A. C. Gossard, and L. A. Coldren, J. Vac. Sci. Technol. **12**, 3075 (1994).
[11] J. Piprek, D. I. Babić, and J. E. Bowers, Appl. Phys. Lett. **68**, 2630 (1996).
[12] G. R. Hadley, K. L. Lear, M. E. Warren, K. D. Choquette, J. W. Scott, and S. W. Corzine, J. Quantum Electron. **32**, 607 (1996).
[13] E. Ahlers, S. F. Helfert, and R. Pregla, Integrated Photonic Research, OSA Techn. Dig. Ser., (OSA, 1996), Vol. 6, p. 340.
[14] ANSYS Release 5.0 (1993) by Swanson Analysis Systems, Inc., Houston, PA.
[15] G. Chen, C. L. Tien, X. Wu, and J. S. Smith, J. Heat Transfer **116**, 325 (1994).
[16] S. Adachi, J. Appl. Phys. **54**, 1844 (1983).
[17] S. Adachi, *Physical Properties of III-V Semiconductor Compounds* (Wiley, New York, 1992).
[18] L. E. Thode, G. Csanak, L. L. So, and T. J. T. Kwan, Proc. SPIE **2146**, 174 (1994).
[19] B. Demeulenaere, B. Dhoedt, S. Goeman, and R. Baets, Integrated Photonic Research, OSA Techn. Dig. Ser., 1996, Vol. 6, p. 336.
[20] L. A. Coldren and S. W. Corzine, *Diode Lasers and Photonic Integrated Circuits* (Wiley, New York, 1995).
[21] J. Piprek, H. Wenzel, and G. Sztefka, Photon. Technol. Lett. **6**, 139 (1994).
[22] M. Afromowitz, Solid State Commun. **15**, 59 (1974).
[23] P. Martin, E. M. Skouri, L. Chusseau, C. Alibert, and H. Bissessur, Appl. Phys. Lett. **l67**, 881 (1995).
[24] D. I. Babic, R. P. Mirin, E. L. Hu, and J. E. Bowers, Electron. Lett. **32**, 319 (1996).
[25] H. G. Grimmeiss and B. Monemar, Phys. Status Solidi **5**, 109 (1971).
[26] B. J. Thibeault, T. A. Strand, T. Wipiejewski, M. G. Peters, D. B. Young, and L. A. Coldren, J. Appl. Phys. **78**, 5871 (1995).
[27] N. M. Margalit, D. I. Babić, K. Streubel, R.P. Mirin, J. E. Bowers, and E. L. Hu, Proceedings of the 15th IEEE International Conference on Semiconductor Lasers, 1996, p. 23.
[28] I. Joindot and J. L. Beylat, Electron. Lett. **29**, 604 (1993).
[29] M. Willatzen, Ph.D. thesis, University of Copenhagen and TFL Hørsholm, Copenhagen, 1993; code modified by M. Ritze, H. Wenzel, and J. Piprek.
[30] S. L. Chuang, Phys. Rev. B **43**, 9649 (1991).
[31] C. G. Van de Walle, Phys. Rev. B **39**, 1871 (1989).
[32] W. van Rossbroek, Bell Syst. Tech. J. **29**, 560 (1950).
[33] ToSCA Release 1992, H. Gajewski, Karl Weierstraβ Institute, Berlin, Germany.
[34] P. A. Andrekson, R. F. Kazarinov, N. A. Olsson, T. Tanbun-Ek, and R. A. Logan, **30**, 219 (1994).
[35] P. J. A. Thijs, L. F. Tiemeijer, J. J. M. Binsma, and T. van Dongen, Philips J. Res. **49**, 187 (1995).